ADDITIVE MANUFACTURING FOR ENERGY APPLICATIONS

On the Thermal Stability of Dislocation Cellular Structures in Additively Manufactured Austenitic Stainless Steels: Roles of Heavy Element Segregation and Stacking Fault Energy

PU DENG,[1] HOUSHANG YIN,[1] MIAO SONG,[2] DIAN LI,[3]
YUFENG ZHENG,[3] BARTON C. PROROK,[1] and XIAOYUAN LOU [1,4]

1.—Department of Mechanical Engineering, Materials Research and Education Center, Auburn University, Auburn, AL 36849, USA. 2.—Nuclear Engineering and Radiological Sciences, University of Michigan, Ann Arbor, MI 48109, USA. 3.—Department of Chemical and Materials Engineering, University of Nevada Reno, Reno, NV 89557, USA. 4.—e-mail: xzl0092@auburn.edu

The thermal stability of dislocation cellular structures in three additively manufactured (AM) austenitic stainless steels (SSs), 316L SS, 304L SS, and Al modified 316L SS (316L(Al)), were studied. Minor alloying elements, Mo and Al, were found affecting the stability of the cellular structures in AM austenitic SS, resulting in a stability ranking of AM 316L SS > AM 304L SS > AM 316L(Al) SS. As a result, their abilities towards recrystallization also differed. Owing to the high stacking fault energy (SFE) due to Al addition, AM 316L(Al) SS had the least stable subgrain cellular structure and exhibited the lowest recovery temperature. Although 316L SS possessed slightly higher SFE than 304L SS, the pinning effect due to Mo segregation at the cellular walls in AM 316L SS significantly enhanced its thermal stability. While the low-SFE AM 316L SS and AM 304L SS recovered their cellular structures via the equiaxed cell growth, the dislocation cellular walls in high-SFE AM 316L(Al) SS continuously vanished along a preferred direction. The fast recovery of cellular structures led to recrystallization retardation. The Hall–Petch model was found incapable of correlating cell size to strength because of the continuous weakening of cellular walls during heat treatment.

INTRODUCTION

Laser powder bed fusion (LPBF) additive manufacturing (AM) has been widely explored as one of the most promising techniques for industries because of its exceptionally high design freedom.[1] Among many distinctive microstructural features in AM stainless steel made by LPBF, the dislocation cellular structure formed during rapid laser solidification was found, enabling superior mechanical properties compared to its conventional counterparts.[2] The dislocation cellular structures consist of high-density cellular walls/boundaries formed by tangled dislocations and dislocation-free interiors, with the average cellular size from 500 nm to 1000 nm depending on the laser processing parameters.[3,4] The partitioning of heavy solute elements on the cellular boundaries, such as Cr and Mo segregation in AM 316L SS[2,5] and Cr and Ni segregation in AM 304L SS,[6–8] was commonly reported. At room temperature, the dislocation cellular structure has demonstrated its effectiveness to strengthen AM austenitic SSs by obstructing dislocation motion (Hall–Petch effect) and also enable superior ductility through the cellular wall-twin interaction.[9] Indirect evidence suggested the segregated elements at the cellular wall stabilize the cellular network at a high strain level by pinning effects.[2]

Compared to the abundant room-temperature data, the thermal stability of the dislocation cellular structures in AM 316L SS at elevated temperatures and the related mechanical responses were less

understood. These data were mostly buried in the scattered literature, with limited experiments being performed for short annealing times at 400–1050°C.[10–13] Quick de-structuring of dislocation cells within 1 h at > 800°C was reported.[10,11,13] Cell stability and its evolution as the function of temperature and time were not established for the intermediate temperature range (400–600°C), which is more valuable for energy applications. Limited data suggested the cellular structures might be stable at up to 800°C.[10,12] The impact of the recovery of dislocation cells on recrystallization was not revealed.

Hierarchical structures, including high-angle grain boundaries and dislocation cellular structures, stored the most energy in AM metals. In conventional rolled/forged alloys, the high-temperature annealing minimizes the free energy through recovery, recrystallization, and grain growth, depending on the temperature.[14] Dislocations rearrange and cross-slip to annihilate during recovery, and excess dislocations form low-angle subgrain boundaries,[15] which share structural similarity to the cellular structures in AM metals. Subgrains that possess high-angle misorientation and exceed critical size have the superiority to grow by consuming stored energy in adjacent grains and subsequently evolve into new defect-free grains, so-called recrystallization.[14] It should be noted that recovery and recrystallization are competitive with each other during annealing.[16] Alloys with unstable dislocation structures may experience easier dislocation recovery and retardation in nucleating new grains.

Among many factors that can affect recovery and recrystallization, stacking fault energy (SFE) is critical to the thermal stability of subgrain dislocation structures.[16,17] For materials with high SFE, the easier dislocation cross-slip facilitates dislocation recovery at lower temperatures, resulting in deficient internal energy and arduous recrystallization.[16] Table I summarizes SFE values for 316-type and 304-type stainless steels measured by different techniques in the literature,[18–28] including (1) spacing measurement between dislocation extended nodes (EN) by transmission electron microscopy (TEM); (2) x-ray diffraction (XRD); (3) neutron diffraction. While data scattered, Table I shows that 316/316L SS generally exhibited higher SFE than 304/304L SS. For many reasons, Al was also added as a minor element in different steels. Pure Al has a very high SFE. It has been extensively shown that adding Al to austenitic steels, e.g., high-Mn twinning-induced plasticity (TWIP) austenitic steels, can increase the SFE.[29–32]

This article seeks to understand the thermal stability of the unique dislocation cellular substructures in AM SSs at elevated temperatures and its effects on recrystallization. By comparing AM austenitic SSs with different minor alloying additions, the study shed lights on the root causes that affected the thermal stability of AM SSs, including the effect of Mo segregation (AM 316L SS versus AM 304L SS) and stacking fault energy (the effect of Al addition). The thermal stability of the dislocation cellular structure of three materials was examined by annealing at 500°C, 600°C, and 700°C with time up to 150 h. Higher temperature heat treatments at 950°C, 1065°C, and 1150°C were also studied to establish the relationship between the thermal stability of cellular structures and recrystallization. The applicability of the Hall–Petch relationship to cellular structure coarsening was also investigated.

Table I. Summary of measured stacking fault energy (SFE) values for 300 series austenitic stainless steels (SSs) from the literature

Metals	SFE, mJ/m^2	Methods
316L	32.8[18]	ND
	25 ± 5[19]	EN
	23 ± 5[20]	EN
	14.2[21]	EN
	30[22]	EN
	36[22]	EN
	53[23]	EN
316	78[23]	XRD
304L	18[23]	XRD
	16.4 ± 1.1[24]	EN
304	30[25]	EN
	17.8 ± 1.2[26]	EN
	28–41[27]	EN
	21[28]	EN

XRD x-ray diffraction, *EN* extended nodes by TEM, *ND* neutron diffraction

MATERIALS AND METHODS

Three types of austenitic SS powders manufactured by nitrogen gas atomization (Carpenter Powder Products) were used in this work. Table II shows the alloy compositions of three as-received powders. 316L SS and 304L SS were utilized to investigate the effect of Mo on the dislocation cell stability, recovery, and recrystallization. A special 316L(Al) SS powder was custom made by replacing Mo with Al and removing Si to examine the role of Al addition. It was expected that Al addition would increase the SFE of 316-type SS, as discussed elsewhere.[29–32] Including 316L(Al) SS in the testing matrix shed light on the impacts of high SFE on dislocation cells due to LPBF.

All three powders with the average size of 10–45 μm were printed with a Concept Laser Mlab LaserCusing® system using the same process parameters: 90 W laser power, 0.6 m/s scan velocity, 25 μm layer thickness, and 80 μm hatching distance. Maintaining the same laser processing parameters was critical to creating similar heat inputs among different materials during LPBF and

Table II. Alloy compositions (wt.%) of as-received austenitic stainless steel powders

wt.%	C	S	P	Mn	Si	Ni	Cr	Mo	Fe	Al
316L	0.024	0.003	0.045	0.79	0.63	12.8	17.8	2.4	Bal	/
316L(Al)	0.0071	0.0039	0.004	1.56	0.03	14.18	17.88	0.14	Bal	0.85
304L	0.015	0.004	0.012	1.4	0.61	9.8	18.4	/	Bal	/

brought a fair comparison on microstructural features.[9] As shown in Table II, the density of AM 316L, AM 304L, and AM 316L(Al) samples, measured based on ASTM E2109, were 99.8%, 99.8%, and 95.4%, respectively. Although the main alloy compositions of three austenitic SS powders were similar, AM 316L(Al) SS had considerably lower density. A separate processing parameter study performed on 316L(Al) SS powder indicated that 99.7% density could be achieved by using a slightly lower energy input (90 W laser power, 0.8 m/s, and 75 μm hatching distance).

AM parts fabricated by three powders were heat-treated for 2 h at 950°C, 1065°C, and 1150°C to explore the degree of recrystallization as a function of temperature. Heat-treated specimens, along with the as-built AM specimens, were sectioned parallel to the build-up direction. The metallographic samples were prepared by mechanically grinding to a 220 grit using SiC grinding paper and then followed by polishing with 9 μm, 3 μm diamond suspension using an auto-polishing machine. The surface was finalized with vibratory polishing using colloidal silica. Backscattered electron (BSE) imaging and energy-dispersive x-ray spectroscopy (EDS) was conducted with an FEI SciosTM 2 DualBeam FIB/SEM at the acceleration voltage of 10 kV. BSE images were used to examine the fraction of recrystallization after heat treatment.

Specimens for transmission electron microscopy (TEM) or scanning TEM (STEM) were prepared using the standard focus ion beam technique in an FEI Helios Nanolab at the Michigan Center for Materials Characterization (MC2) at the University of Michigan. The FIB lift-outs were first thinned to around $\sim$ 300 nm by 30 keV beam energy and then to about $\sim$ 100 nm by 5 keV to reduce the FIB damages. Energy-dispersive x-ray spectroscopy (EDS) mappings were performed on a Thermo Scientific Talos F200X microscope operating at 200 kV. EDS-based hypermaps were taken with 512 × 512 pixels using a probe full-width half maximum of $\sim$ 1.5 nm and a beam current of around 3 nA. After collecting the hypermaps, line scanning data can be generated between any two points within the 2D map using Velox software.

Thermal stability of cellular structures in AM specimens was studied by vacuum-annealing at 500°C, 600°C, and 700°C for 10 h, 24 h, 48 h, and 100 h. All annealed and as-built AM SS specimens were examined on the faces perpendicular to the build-up direction to better reveal the dislocation cellular structures. The samples were prepared using the same polishing procedure described above to produce a scratch-free surface. To best reveal the dislocation cellular structures, AM 316L SS specimens were then etched using mixed acids (HCl: HNO_3: H_2O = 4:1:3) by immersion for 75 s, by which the interior of the cellular structure was etched away. For AM 304L SS and AM 316L(Al) SS, the mixed acid method did not bring up the contrast for dislocation cells. Instead, the electro-etching for 15 s using 10% oxalic acid at 15 V DC voltage was adopted for AM 304L and AM 316L(Al). With electro-etching, the cellular boundaries were absent. Figure 1 shows the morphology differences by different etching methods. The cellular structure was examined by SEM under secondary electron (SE) mode. The average cellular size was measured by the intercept method using ImageJ. Eight SEM micrographs were measured for each specimen.

Vickers hardness test was performed using a DM-400 FT Microhardness Tester (LECO Corp.) with an applied force of 1 kg and a duration time of 25 s. Seven indentations were made on each specimen, and the average hardness along with deviation was reported.

RESULTS AND DISCUSSION

Coarsening of Dislocation Cellular Structures as a Function of Temperature and Time

Figure 1 shows the evolution of dislocation cellular structures as the functions of temperature and time in AM 316L SS, AM 304L SS, and AM 316L(Al) SS. The comparisons among the three different materials were purposely designed to evaluate the impacts from the additions of Mo (316L versus 304L) and Al (304L versus 316L(Al)) on recovery and recrystallization in AM austenitic SS. At 600°C for up to 100 h (Fig. 1a), the cellular structures in AM 316L SS and AM 304L SS exhibited prominent thermal stability, though a minimal amount of cellular walls started to vanish in AM 304L SS after 10 h annealing. It is worth noting that chromium carbide precipitation was observed in AM 304L SS annealed at 600°C for 100 h, which was confirmed by EDS/SEM in Fig. 2. In comparison, the destruction of cellular structures in AM 316L(Al) SS began after 10 h annealing at 600°C. The SEM micrographs of AM 316L(Al) SS in Fig. 1a showed the evolution of cellular morphology at 600°C, which showed that the annihilation of cellular walls was prone along a particular orientation.
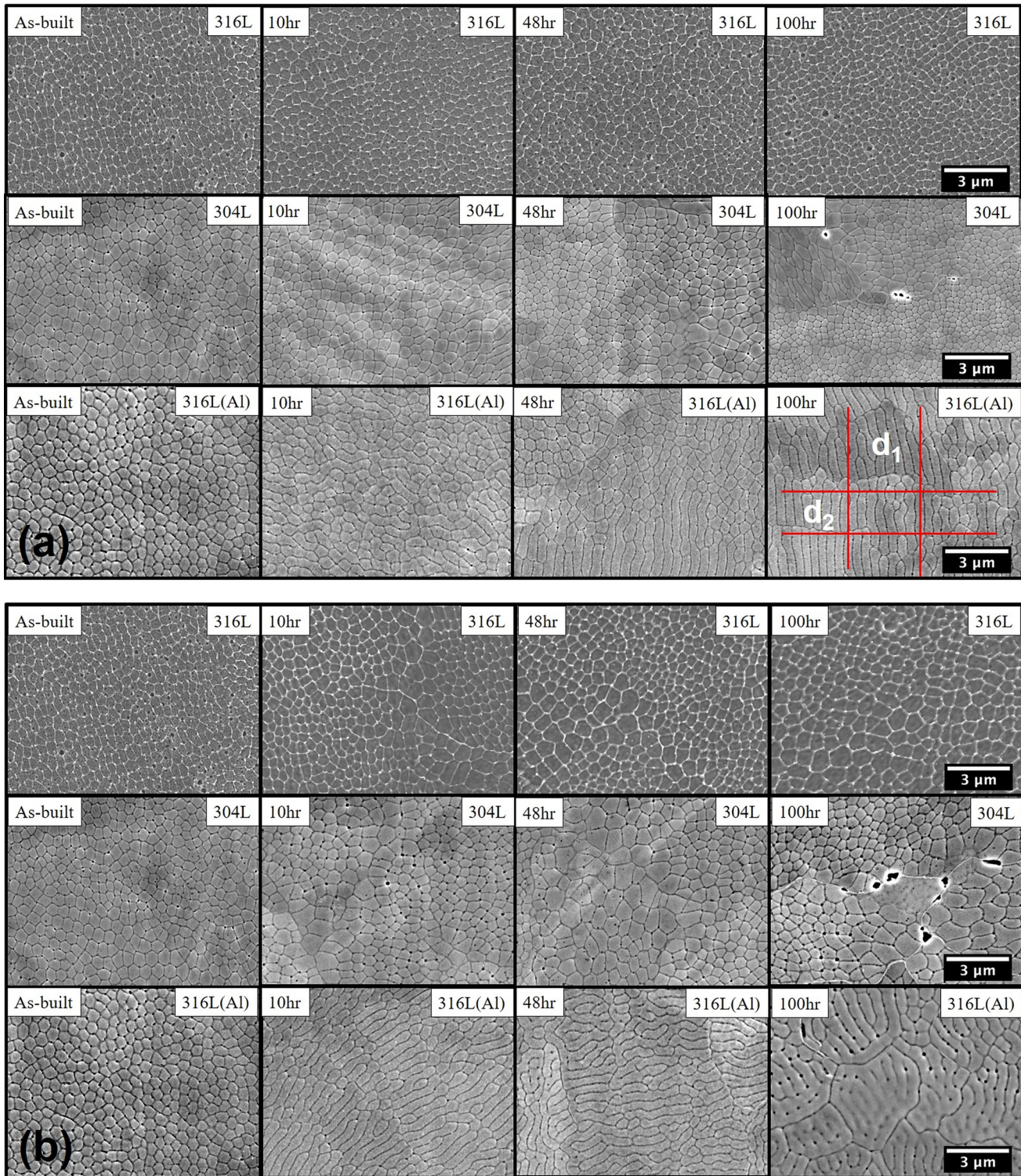
Fig. 1. Etched SEM micrographs of AM 316L SS, AM 304L SS, and AM 316L(Al) SS, showing cellular structure at the horizonal plane (perpendicular to the build-up direction). Three materials were annealed at (a) 600°C and (b) 700°C for 10 h, 24 h (not displayed), 48 h, and 100 h (Color figure online).

As a result, the equiaxed cell morphology was converted to rod-like cells with a large aspect ratio. Chromium carbide precipitation was also observed in AM 316L(Al) SS annealed at 600°C for 100 h. Carbides in AM 316L(Al) SS were more prevalent than those in AM 304L SS. It is known that the kinetics of carbide nucleation and growth highly depends on subtle differences in microstructure/microchemistry, such as grain boundary misorientation,[33,34] dislocation density,[33] minor alloying
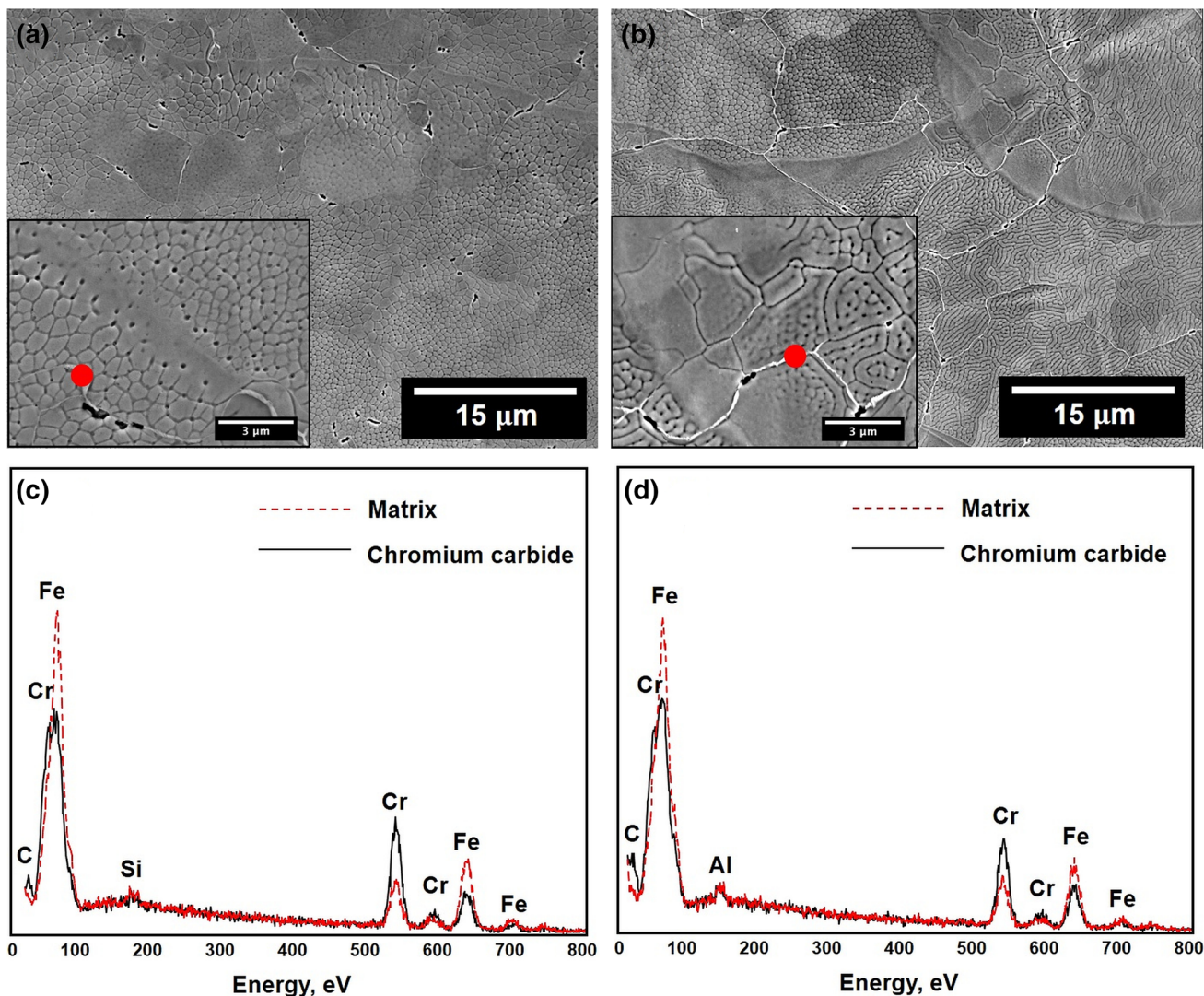
Fig. 2. Etched SEM image and EDS spectrum of chromium carbide at the high-angle grain boundary for of AM 304L SS (a and c) and AM 316L(Al) SS (b and d) annealed at 700°C for 100 h. The same but fewer chromium carbides were observed at 600°C for 100 h for both materials. Red dots represent point analysis of EDS (Color figure online).

elements,[35] and so on. For instance, in conventional forged products, a high density of dislocation by cold work can promote carbide nucleation at a lower temperature.[36,37] Also, the addition of Mo can inhibit carbide nucleation in L-grade SSs.[38] Therefore, future investigation is needed to elucidate the cause of different carbide precipitation kinetics in these materials. Since AM 316L(Al) showed the most unstable cellular structure among three materials, annealing at 500°C was also conducted in this study, which confirmed the destruction of dislocation cells in AM 316L(Al) SS could be initiated after 24 h annealing at 500°C.

At 700°C, in Fig. 1b, the dislocation cells in all three materials decomposed to varying degrees after 10 h annealing. However, the cells evolved in different manners. For AM 316L SS and AM 304L SS, the dislocation cells grew uniformly along all directions through the rearrangement and coarsening of dislocation substructures. The coarsening rate was location-dependent. In AM 304L SS, the disappearance of cellular walls was also visible at 48 h and 100 h. Thermally activated dislocation–dislocation interactions eliminated cellular boundaries at a higher temperature. In AM 316L(Al) SS, a large number of cellular walls vanished along a certain direction after 10 h annealing, leaving the material maze-like structure. With a minimum amount of rearrangement and coarsening in dislocation cells, the disappearance of cellular walls along a certain direction turned cells into rod-like shapes. At 100 h, in AM 316L(Al) SS, most cellular walls disappeared, leaving the material with mostly high-angle boundaries. Recrystallization was not observed in all samples in Fig. 1a and b.

Evolutions of Cellular Size and Hardness

The changes in cell size and hardness are shown in Fig. 3. For AM 316L SS and AM 304L SS, the cell size was calculated by the average boundary spacing following the linear intercept method defined in ASTM E112. For AM 316L(Al) SS, the method used by Kamikawa et al.[39] to determine the boundary spacing of elongated subgrain cells after rolling was adopted in this work. Two sets of mutually perpendicular lines, as shown by the red lines in Fig. 1a, were drawn, and the boundary spacing was calculated by the linear intercept method for each line. The average cell size was calculated by the following equation:

$$d = \frac{2}{\frac{1}{d_1} + \frac{1}{d_2}} \tag{1}$$

where d_1 is the average size measured by the line parallel to the long edge of the cells, and d_2 is the average size measured by the line perpendicular to the long edge of the cells.

In Fig. 3a, AM 316L SS and AM 304L SS exhibited a similar average cell size of $\sim 0.41\ \mu$m in all tested conditions, indicating their good thermal stability at 600°C. The stable cellular structures of AM 316L SS and AM 304L SS were also demonstrated by the steady hardness values shown in Fig. 3c in all annealing treatments. In comparison, AM 316L(Al) SS, at 600°C, showed the continuous destruction of dislocation cellular structure over time, which led to an increase in average cell size in Fig. 3a and the corresponding decrease in hardness, as displayed in Fig. 3c. At 700°C, a slight increase of cell size was also shown in AM 316L SS (Fig. 3b) because of regional cell coarsening, resulting in a stable descent of hardness in Fig. 3d. The hardness of AM 316L SS was reduced from 230.6 to 221 HV after 100 h annealing at 700°C. On the other hand, cell coarsening in AM 304L SS was observed after 10 h annealing at 700°C. Noticeable changes in cell size (Fig. 3b) and hardness (Fig. 3d) were observed after 100 h annealing because of the large-area cell wall vanishing as shown in Fig. 2b. Compared to AM 316L SS and AM 304L SS, AM 316L(Al) SS exhibited
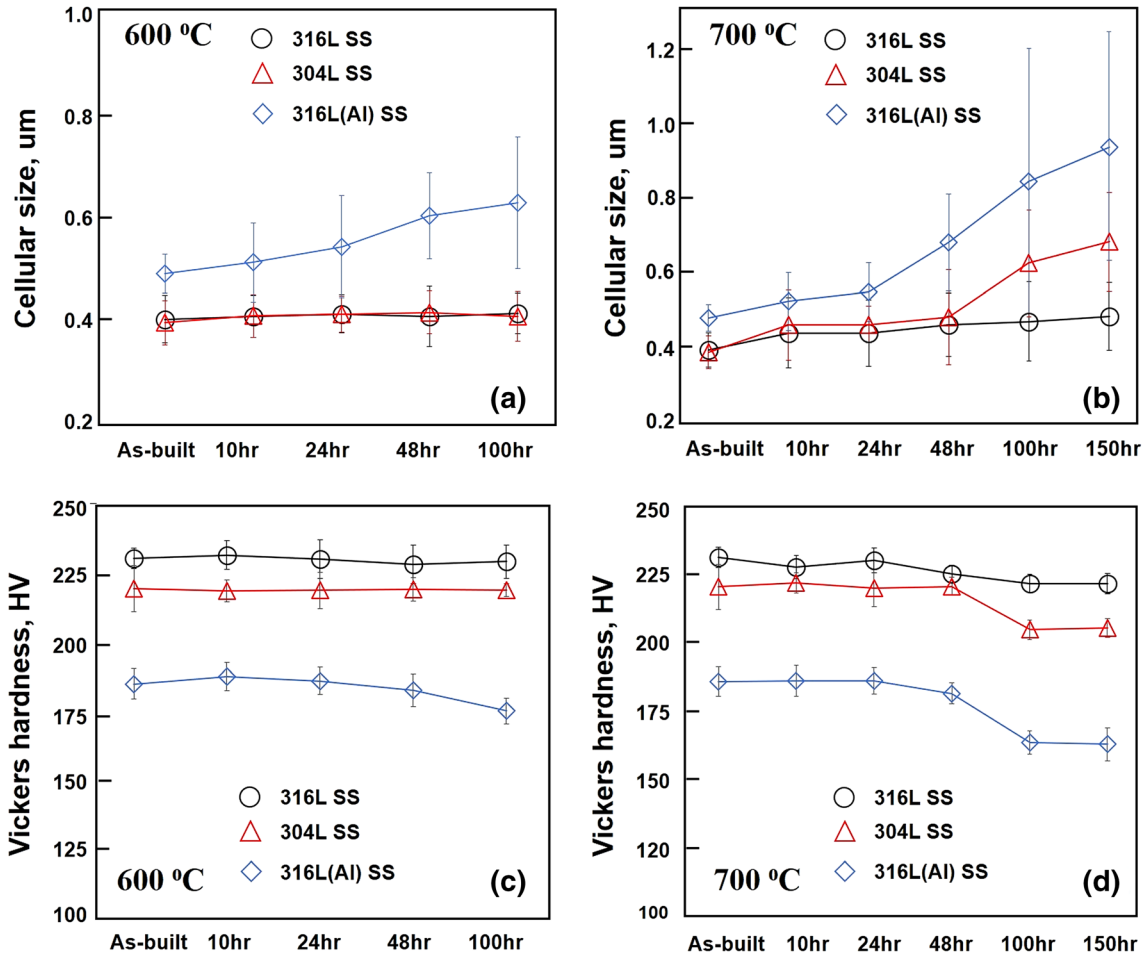

Fig. 3. Cellular size (a and b) and Vickers hardness (c and d) of as-built and annealed AM 316L stainless steel (SS), AM 304L SS, and AM 316L(Al) SS at 600°C for 10–100 h, (a) and (c); and 700°C, (b) and (d) for 10–150 h, respectively. The cellular size was analyzed by the intercept method using an etched SEM micrograph at the plane perpendicular to the build-up direction (Color figure online).

more prominent cell coarsening and hardness reduction in all testing conditions. The 150 h annealing was also studied for 700°C annealing. At 700°C, after 100 h, though the dislocation cell size continued to increase over time, the hardness of all three materials did not further decrease. The inconsistent trend after 100 h suggested the characteristics of the cellular walls evolved. Its resistance to dislocation movement was degraded because of the recovery of dislocations along the walls. Carbide formation may also improve the strength. However, carbides mostly precipitated out along high-angle grain boundaries in all three materials. Previous studies confirmed the hardness (initial stages of plasticity) in AM 316L SS was dominated by the spacings of subgrain cellular structures.[40] Thus, carbides were less likely to interact with dislocations when subgrain cellular structures were present.

TEM Characterization of Dislocation Cellular Structures

TEM characterization of cellular structures in as-built AM 316L SS and as-built AM 316L(Al) SS are shown in Fig. 4. It should be mentioned that a similar amount of dispersed oxide inclusions (40–80 nm) were also identified in both materials.[5] The inclusions in AM 316L SS were rich in Si and Mn, while those in AM 316L(Al) SS were rich in Al, given the fact that Al has the highest oxygen affinity, among other alloying elements. The cellular walls in both materials were composed of tangled dislocations due to local strain mismatch during rapid solidification. The spread of dislocations near the walls suggested the elastic interactions among dislocations with different signs controlled the wall thickness. Based on the TEM characterization in this study, it
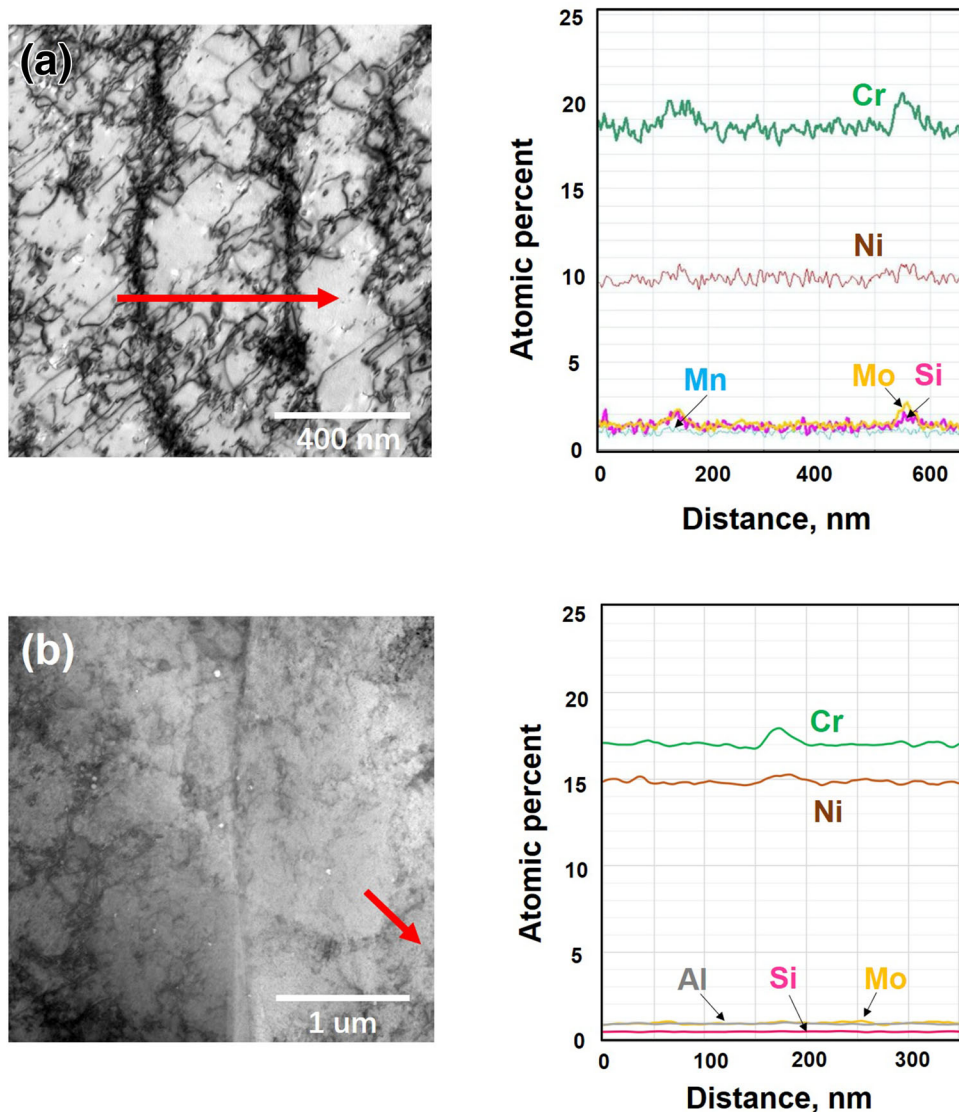

Fig. 4. TEM image and EDS line scan of the cellular boundary showing the elemental segregation at the cellular wall of (a) AM 316L(Al) SS and (b) AM 316L(Al) SS. Red arrows represent the EDS line scan location (Color figure online).

seemed that AM 316L SS exhibited higher dislocation density than AM 316L(Al) SS, probably owing to the high SFE from the Al addition that enabled the high dislocation mobility. It should be noted that TEM samples of AM 316L SS and AM 316L(Al) SS were prepared differently. The AM 316L SS was thinned by jet polishing, while the AM 316L(Al) SS was done by FIB. Jet polishing generally resulted in a better quality view of the dislocation substructures in AM SS. However, due to the slightly higher porosity of AM 316L(Al) SS, jet polishing could not resolve enough thin area. Therefore, the observed difference in dislocation density needs further experimental confirmation. The EDS line scan on the cellular wall indicated the Cr and Mo segregation on the cellular walls in AM 316L SS as well as Cr and Ni segregation on the cellular walls in AM 316L(Al) SS. The elemental segregation of AM 304L SS has been widely reported as Cr and Ni were found to segregate at cellular walls, like AM 316L(Al) SS.[6–8] Figure 1 has demonstrated a cellular thermal stability ranking of AM 316L SS > AM 304L SS > AM 316L(Al) SS. At 700°C, dislocation cells in AM 304L SS and AM 316L(Al) SS begin to vanish after 100 h annealing, while the cells in AM 316L SS were still robust. Thus, this study confirmed the pinning effects of Mo in AM 316L SS are the primary reason for its higher thermal stability.

Feasibility of the Hall–Petch Relationship on Dislocation Cell Coarsening

The strength of metallic materials can be expressed as follows:

$$\sigma_y = \sigma_0 + \sigma_{dis} + \sigma_{gb} + \sigma_{ppt} \qquad (2)$$

where σ_0 is the friction stress, σ_{dis} is the contribution from dislocations, σ_{gb} is the contribution from grain boundaries, and σ_{ppt} is the contribution from precipitation. In AM SSs by LPBF, the unique dislocation cellular structures were formed by low-angle cellular walls composed of high-density tangled dislocations and dislocation-free cell interiors, as shown in Fig. 4. It is reasonable to assume the dislocation strengthening in AM materials originated from dislocation cellular walls. With low annealing temperature, no recrystallization occurred. Thus, high-angle grain boundaries remain unchanged. Precipitation strengthening due to chromium carbide formation was also negligible, evidenced by the low carbon content in Table II and softening in Fig. 3c and d. Therefore, the yield strength can be directly correlated to the cellular size based on the Hall–Petch relationship:

$$\sigma_y = \sigma_0 + kd^{-1/2} \qquad (3)$$

where k is the Hall–Petch coefficient, and d is the average size of cells. This approach was proven valid elsewhere.[2, 39, 41] Extensive work has been done to correlate σ_y to the Vickers hardness value.
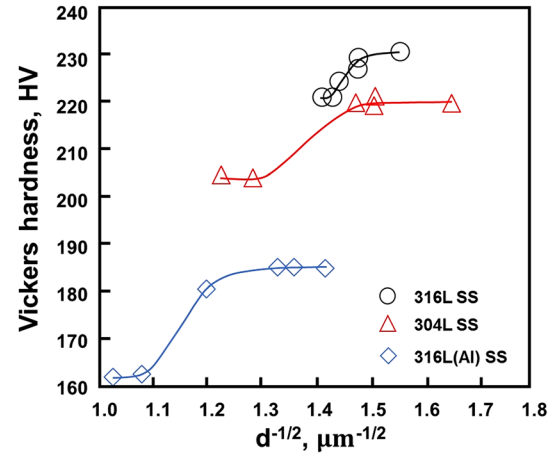

Fig. 5. Vickers hardness versus $d^{-1/2}$, where d is the cellular size, of AM 316L stainless steel (SS), AM 304L SS, and AM 316L(Al) SS annealed at 700°C for 10–150 h. The lines were not fitted curves. They were presented only to visualize the overall trend (Color figure online).

For cold-worked austenitic stainless steels, it was agreed that σ_y (MPa) could be estimated proportional to the Vickers hardness value (HV).[42–44] Therefore, by direct translation, HV can also be proportional to $d^{-1/2}$, where d is the cellular size, given in the following relationship.

$$HV = A + Bd^{-1/2} \qquad (4)$$

where A and B are constant. Figure 5 plots the HV versus $d^{-1/2}$ relationship for all three materials. A linear relationship cannot be established for all three materials at different temperatures. However, the general trend was similar. At the initial stage of annealing (< 48 h), the strengthening coefficient B was small in all three materials (< 30), slightly lower than other reported Hall–Petch fitting of LPBF AM 316L SS in the literature.[10] We concluded a pseudo Hall–Petch relationship of cellular rearrangement and coarsening was present at the early stage. A sharp decrease in HV between 48 and 100 h broke the linear trend, implying significant changes in the characteristics of dislocation cellular walls took place at this time. Dislocation cellular structures in AM SS were observed unstable at higher temperatures.[11] Dislocation annihilation on cellular walls was observed at > 800°C.[10] Figure 5 confirmed that dislocation annihilation could happen on cellular walls at lower temperatures, and as a result, the cellular walls' ability to restrain the dislocation movement decreased. Interestingly, three AM SSs annealed at 700°C for 150 h exhibited no further reduction of hardness. At the early stage of recovery, dislocations with conflicting signs were annihilated; thus, the dislocation density decreased. Excess dislocations rearranged themselves in sub-grain boundaries, forming more stable interfaces. These processes led to the slowdown of dislocation recovery, which may contribute to the flattening
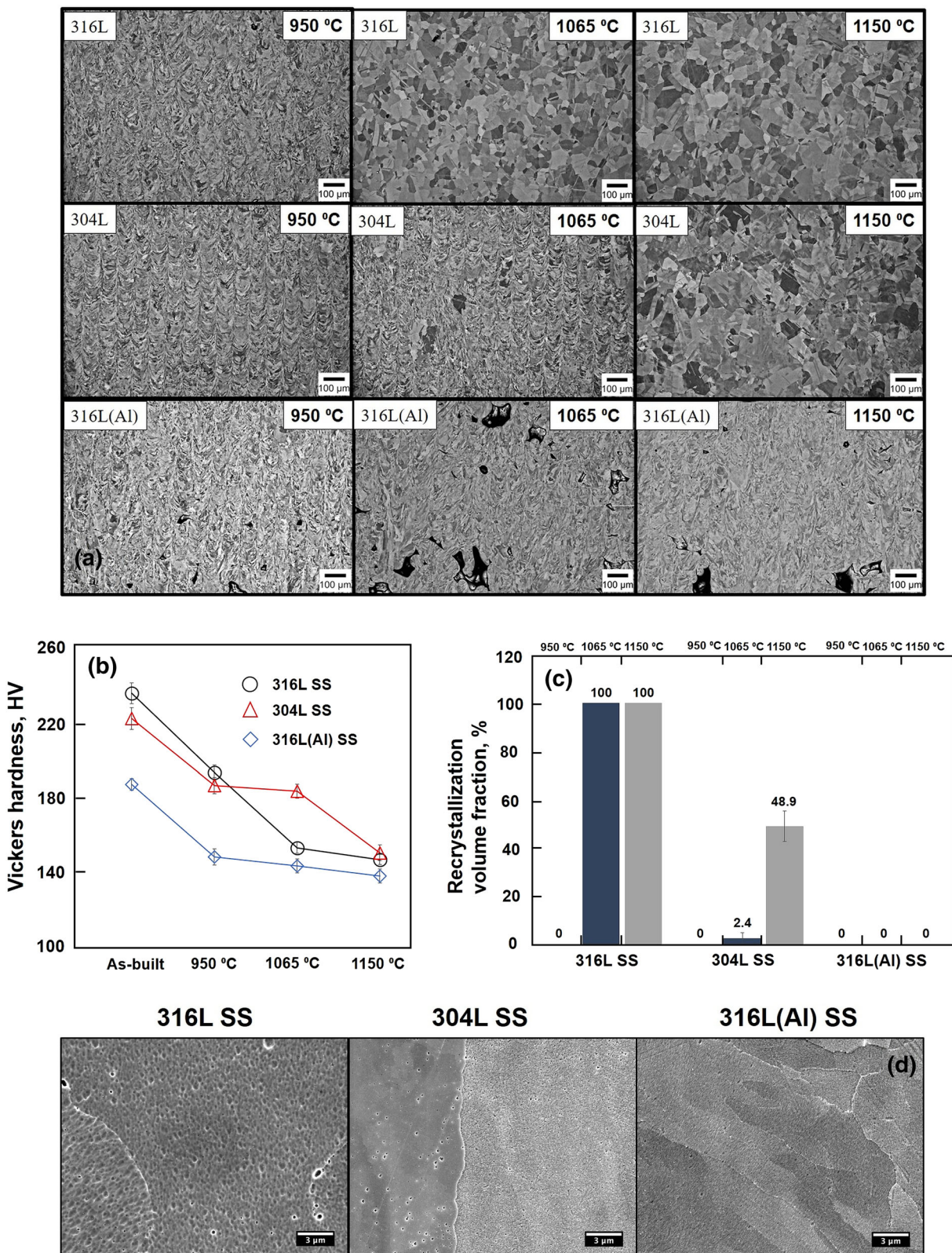
Fig. 6. (a) Back-scattered electron (BSE) images, (b) Vickers hardness, and (c) recrystallization volume fraction of AM 316L stainless steel (SS), AM 304L SS, and AM 316L(Al) SS heat-treated at 950°C, 1065°C, and 1150°C for 2 h, (d) etched SEM micrographs of AM AM 316L stainless steel (SS), AM 304L SS, and AM 316L(Al) SS heat-treated at 950°C for 0.5 h (Color figure online).

trend in hardness after 100 h annealing. Carbide formation (shown in Fig. 2) may also improve the strength. However, carbides were mostly observed along high-angle grain boundaries. Thus, their contribution, if existed, was limited to pinning grain boundaries. Carbides were less likely to affect dislocations or interact with dislocation movements.

Effects of Dislocation Cell Thermal Stability on Recrystallization

The thermal stability of dislocation cellular structures in AM SSs was directly linked to the material's ability to recrystallize. Figure 6a exhibits the general looks of the grain structures in three materials after being heat-treated at 950°C, 1065°C, and 1150°C for 2 h. The Vickers hardness and fraction of recrystallization in as-built and heat-treated specimens are displayed in Fig. 6b and c. AM 316L SS showed the lowest recrystallization temperature among the three. Full recrystallization (100%) was achieved at 1065°C and 1150°C. In comparison, AM 304L SS showed partial recrystallization (48.9%) at > 1150°C, and no recrystallization was observed in AM 316L(Al) SS at all temperatures. Under the as-built condition, AM 316L SS exhibited the highest HV among three materials, primarily attributed to the solute hardening by Mo. After being heat-treated at 950°C for 2 h, the hardness of all three materials decreased to a similar extent because of the significant reduction in dislocation density. Etching did not reveal cellular structures in all three samples heat-treated at 950°C for 0.5 h, as demonstrated in Fig. 6d, confirming the complete elimination of cellular structures at this temperature. While no prominent hardness change was observed in AM 316L(Al) SS at higher temperatures, AM 316L SS and AM 304L SS exhibited another significant hardness drops at 1065°C and 1150°C, respectively, directly corresponding to the start of recrystallization. The grain growth in the fully recrystallized AM 316L SS, from 34.5 μm (1065°C) to 45.3 μm (1150°C), resulted in a similar level of hardness decrease like that in the un-recrystallized AM 316L(Al) SS at the same temperature range. It is worth noting that the recovery of dislocation cellular structures in AM austenitic SSs was responsible for the same level of hardness change as recrystallization, which indirectly evidenced the high amount of free energy that was stored by dislocation cells in AM materials. Figure 6 shows that the ability to recrystallize in AM austenitic SSs was controlled by the thermal stability of dislocation cellular structures. Fast recovery in AM 316L(Al) SS resulted in the retardation of recrystallization.

Mechanistic Implications on Dislocation Cellular Structures in AM Stainless Steels

According to Table I, the SFE of 316L SS is generally higher than that of 304L SS. Moreover,

Rhodes et al. reported that the SFE increases with increasing Ni content in the Fe-18 wt.%Cr-Ni system.[45] Table II shows that the 316L SS has a similar amount of Cr (approximately 18 wt.%), but lower Ni content compared to 304L SS. Mo was also reported to increase the SFE of Fe-Cr-Ni austenitic stainless steel.[46] Therefore, the SFE of AM 316L SS is expected to be higher than AM 304L SS in the present work. With the higher SFE and thus higher dislocation mobility, the dislocation substructures in AM 316L SS were expected to rearrange and be annihilated more easily than AM 304L SS during the recovery process. However, this is in contradiction to the experimental observation in this study. TEM evidence in Fig. 4 confirmed the Mo segregation along with the dislocation cellular walls in AM 316L SS. Therefore, the pinning effects by heavy elemental segregation, e.g., Mo, were experimentally confirmed to play a critical role in the thermal stability of the cellular structures in AM metals by LPBF.

Pure Al intrinsically exhibited very high SFE. It has been extensively shown that Al addition in austenitic steels, such as high-Mn twinning-induced plasticity (TWIP) steels, can increase the SFE.[29–32] In addition, Si was reported to decrease the SFE of austenitic TWIP steels.[29,32] The addition of Al and the lack of Si combined, compared to AM 316L SS, had a tendency to significantly increase the overall SFE of AM 316L(Al) SS. Though this study did not measure SFE, it is reasonable to expect the SFE of AM 316L(Al) SS was the highest among the three SSs. Considering the similar elemental segregation (Cr and Ni) on the cellular walls in AM 316L(Al) SS and AM 304L SS, the distinct thermal instability in AM 316L(Al) was attributed to its high SFE.

The elimination of cellular walls in three AM SSs during recovery proceeded in different manners. The low-SFE AM 316L SS and AM 304L SS recovered their cellular structures via the equiaxed cell growth, while the cellular walls in high-SFE AM 316L(Al) SS continuously vanished along a preferred direction. During the recovery of AM 316L SS and AM 304L SS, the cellular wall, also considered a low-angle boundary, further reduced the total free energy by rearranging its orientation and coarsening. Eventually, the boundaries of the coarsened cells disappeared because of the de-structuring of the tangled dislocations. The notable de-structuring was generally promoted by higher energy input (> 700°C). In high-SFE AM 316L(Al) SS, much lower input energy was needed to initiate the continuous vanishment of cellular walls. We observed the de-structuring of cellular walls along a particular direction in AM 316L(Al) SS at 500°C. We believe the unique directional recovery of cellular walls in AM 316L(Al) SS was contributed by the high SFE and the respective crystallographic orientations in those grains. High SFE leads to higher dislocation mobility and easier cross-slip. It is worth noting AM SS generally exhibits texture in specific orientations (usually the build direction). The relative orientation among

individual dislocations, dislocation walls, and crystallographic orientations may result in the cross-slip and promote dislocation recovery along certain directions. Further characterizations of the crystallographic orientation relationship are needed to reveal the underlying mechanisms.

CONCLUSION

The thermal stability of the dislocation cellular structures in three additively manufactured austenitic SSs were investigated as a function of temperature and annealing time. By purposely selecting the chemistry of austenitic SSs, the study aimed to provide mechanistic insights into the root causes of the thermal stability of dislocation substructures formed by LPBF. Experimental evidence confirmed the critical roles of the segregation of heavy elements (e.g., Mo) and SFE (controlled by Al addition) in the stability of dislocation cells in AM materials, which was found to further affect the materials' ability towards recrystallization. The detailed summary of the conclusion is listed as follows.

(1) Among three SSs being studied, the thermal stability of dislocation cellular structures was ranked as AM 316L SS > AM 304L SS > AM 316L(Al) SS. The notable destruction of cellular walls was observed to begin at 700°C in AM 316L SS, 600°C, in AM 304L SS and 500°C in AM 316L(Al) SS. At temperatures > 900°C, the dislocation substructures vanished quickly for very short exposure. While AM 316L SS and AM 304L SS reduced the cellular walls through equiaxed cell coarsening, AM 316L(Al) SS exhibited a distinctive cellular wall elimination along a preferred orientation.

(2) Heavy elemental segregation on dislocation cellular walls, e.g., Mo in AM 316L SS, was confirmed to enhance the thermal stability of cellular substructures in AM austenitic SSs that were produced by LPBF. Higher thermal stability in AM austenitic SS resulted in lower recrystallization temperature.

(3) High SFE, promoted by Al addition, can decrease the dislocation density on cellular walls in the as-built material and significantly reduce the thermal stability of the dislocation cellular structures in AM austenitic SS. Recrystallization cannot be achieved in high-SFE AM 316L(Al) SS because of its quick recovery at high temperatures.

(4) Notable carbide nucleation was observed at 600°C in AM 304L SS and AM 316L(Al) SS, but not in AM 316L SS. At 700°C, carbide precipitation was present in all three AM SSs.

(5) Recovery (the destruction of cellular walls) stood in opposition to the recrystallization in AM SSs. The fast recovery of cellular substructures led to the recrystallization retardation. While recovery and recrystallization both contributed to hardness reduction, it is worth noting their contributions to hardness reduction were at a similar level in AM austenitic SS.

(6) The Hall–Petch relationship was found incapable of correlating cellular size to strength during dislocation cell coarsening because of the continuous weakening of cellular boundaries during heat treatment.

CONFLICT OF INTEREST

On behalf of all authors, the corresponding author states that there is no conflict of interest.

REFERENCES

1. T. DebRoy, H.L. Wei, J.S. Zuback, T. Mukherjee, J.W. Elmer, J.O. Milewski, A.M. Beese, A. Wilson-Heid, A. De, and W. Zhang, *Prog. Mater. Sci.* 92, 112 (2018).
2. Y.M. Wang, T. Voisin, J.T. McKeown, J. Ye, N.P. Calta, Z. Li, Z. Zeng, Y. Zhang, W. Chen, T.T. Roehling, R.T. Ott, M.K. Santala, P.J. Depond, M.J. Matthews, A.V. Hamza, and T. Zhu, *Nat. Mater.* 17, 63 (2018).
3. Y. Zhong, L. Liu, S. Wikman, D. Cui, and Z. Shen, *J. Nulc. Mater.* 470, 170 (2016).
4. R. Casati, J. Lemke, and M. Vedani, *J. Mater. Sci. Technol.* 32, 738 (2016).
5. P. Deng, M. Karadge, R.B. Rebak, V.K. Gupta, B.C. Prorok, and X. Lou, *Addit. Manuf.* 35, 101334 (2020).
6. M. Ghayoor, K. Lee, Y. He, C.-H. Chang, B.K. Paul, and S. Pasebani, *Addit. Manuf.* 32, 1 (2020).
7. M.A. Melia, H.-D.A. Nguyen, J.M. Rodelas, and E.J. Schindelholz, *Corros. Sci.* 152, 20 (2019).
8. W. Huang, Y. Zhang, W. Dai, and R. Long, *Mater. Sci. Eng., A* 758, 60 (2019).
9. L. Liu, Q. Ding, Y. Zhong, J. Zou, J. Wu, Y.-L. Chiu, J. Li, Z. Zhang, Q. Yu, and Z. Shen, *Mater. Today* 21, 354 (2018).
10. P. Krakhmalev, G. Fredriksson, K. Svensson, I. Yadroitsev, I. Yadroitsava, M. Thuvander, and R. Peng, *Metals* 8, 643 (2018).
11. E. Tascioglu, Y. Karabulut, and Y. Kaynak, *Int. J. Adv. Manuf. Technol.* 107, 1947 (2020).
12. N. Chen, G. Ma, W. Zhu, A. Godfrey, Z. Shen, G. Wu, and X. Huang, *Mater. Sci. Eng., A* 759, 65 (2019).
13. M.L. Montero Sistiaga, S, Nardone, C. Hautfenne, and J. Van Humbeeck, in *Proc. Annu. Int. 27th* 558 (2016).
14. D.A.H.R.D. Doherty, F.J. Humphreys, J.J. Jonas, D. Juul-Jensen, M.E. Kassner, W.E. King, T.R. McNelley, H.J. McQueen, and A.D. Rollett, *Mater. Sci. Eng. A* 238, 219 (1997).
15. I.Z. Awan and A.Q. Khan, *J. Chem. Soc. Pak.* 41, 1 (2019).
16. P.A.F. Stüwe and H.P.F. Siciliano Jr, *Mater. Sci. Eng. A* 333, 361 (2002).

17. N. Peranio, Y.J. Li, F. Roters, and D. Raabe, *Mater. Sci. Eng., A* 527, 4161 (2010).
18. W. Woo, J.S. Jeong, D.K. Kim, C.M. Lee, S.H. Choi, J.Y. Suh, S.Y. Lee, S. Harjo, and T. Kawasaki, *Sci. Rep.* 10, 1350 (2020).
19. X. Feaugas and C. Gaudin, *Int. J. Plast* 20, 643 (2004).
20. J.I.P. Bampton and M.H. Loretto, *Acta Metall.* 26, 39 (1978).
21. D. Molnár, X. Sun, S. Lu, W. Li, G. Engberg, and L. Vitos, *Mater. Sci. Eng. A* 759, 490 (2019).
22. P.R. Swann, *Corrosion* 19, 102t (1963).
23. R.R.P. Schramm, *Metall. Mater. Trans. A* 6, 1345 (1975).
24. R.A.W. Latanision, *Metall. Mater. Trans. B* 2, 505 (1971).
25. M.J. Whelan, P.B. Hirsch, R.W. Horne, and W. Bollmann, *Proc. R. Soc. Lond. Ser. A. Math. Phys. Sci* 240, 524 (1957).
26. S. Curtze, V.T. Kuokkala, A. Oikari, J. Talonen, and H. Hänninen, *Acta Mater.* 59, 1068 (2011).
27. T.G. Douglass and W.R. Roser, *Corrosion* 20, 15 (1964).
28. L.E. Murr, *Thin Solid Films* 4, 389 (1969).
29. G.R. Lehnhoff, K.O. Findley, and B.C. De Cooman, *Scr. Mater.* 92, 19 (2014).
30. J. Kim, S.-J. Lee, and B.C. De Cooman, *Scr. Mater.* 65, 363 (2011).
31. K.-T. Park, K.G. Jin, S.H. Han, S.W. Hwang, K. Choi, and C.S. Lee, *Mater. Sci. Eng., A* 527, 3651 (2010).
32. E.S. Essoussi and E. Essadiqi, *Procedia Manuf.* 22, 129 (2018).
33. S.M. Bruemmer, *Corrosion* 46, 699 (1990).
34. B.W. Bennett and H.W. Pickering, *Metall. Mater. Trans. A* 18, 1117 (1991).
35. R. Pascali, A. Benvenuti, and D. Wenger, *Corrosion* 40, 21 (1984).
36. R. Singh, I. Chattoraj, A. Kumar, B. Ravikumar, and P.K. Dey, *Metall. Mater. Trans. A* 34, 2441 (2003).
37. S.K. Mannan, R.K. Dayal, M. Vijayalakshmi, and N. Parvathavarthini, *J. Nucl. Mater.* 126, 1 (1984).
38. P.L. Andresen, *Understanding and Mitigating Ageing in Nuclear Power Plants* (Philadelphia: Woodhead Publishing, 2010), pp. 236–307.
39. N. Kamikawa, T. Hirochi, and T. Furuhara, *Metall. Mater. Trans. A* 50, 234 (2018).
40. T. Pinomaa, M. Lindroos, M. Walbrühl, N. Provatas, and A. Laukkanen, *Acta Mater.* 184, 1 (2020).
41. E. Getto, B. Tobie, E. Bautista, A.L. Bullens, Z.T. Kroll, M.J. Pavel, K.S. Mao, D.W. Gandy, and J.P. Wharry, *JOM* 71, 2837 (2019).
42. J.R. Cahoon, W.H. Broughton, and A.R. Kutzak, *Metall. Trans.* 2, 1979 (1971).
43. O. Takakuwa, Y. Kawaragi, and H. Soyama, *J. Surf. Engd. Mater. Adv. Technol.* 03, 262 (2013).
44. J.T. Busby, M.C. Hash, and G.S. Was, *J. Nucl. Mater.* 336, 267 (2005).
45. C.G. Rhodes and A.W. Thompson, *Metall. Trans. A* 8, 1901 (1977).
46. T. Yonezawa, K. Suzuki, S. Ooki, and A. Hashimoto, *Metall. Mater. Trans. A* 44, 5884 (2013).